



Surface radiation balance in the ablation zone of the west Greenland ice sheet

Michiel van den Broeke,¹ Paul Smeets,¹ Janneke Ettema,¹ and Peter Kuipers Munneke¹

Received 15 August 2007; revised 5 February 2008; accepted 21 February 2008; published 3 July 2008.

[1] We present 4 years of radiation observations and derived cloud properties from the ablation zone of the west Greenland ice sheet (67°N). Data were collected using three automatic weather stations located at 6, 38, and 88 km from the ice sheet margin at elevations of 490, 1020, and 1520 m asl. This part of Greenland is characterized by a ~150 km wide tundra, a ~100 km wide ablation zone and an average equilibrium line altitude of ~1500 m asl. At the lowest station, snow is redistributed by the wind in crevasses and gullies, leading to very little measured winter accumulation. As a result, glacier ice (albedo ≈ 0.55) is at the surface throughout the melting season. At 1020 m asl, the winter snow cover typically disappears in mid to end June. At 1520 m asl, superimposed ice briefly reaches the surface at the end of the ablation season. The combined effect of decreasing surface albedo and increasing cloud optical thickness as summer progresses causes absorbed shortwave radiation to peak in June at low elevations but progressively later at higher elevations. Incoming longwave radiation peaks in August, in response to increased cloud optical thickness and heating of the atmosphere over the snow and ice-free surroundings. The ice sheet margin experiences continuous melting in June, July, and August. This limits the emission of longwave radiation, causing net longwave radiation to peak in August, further enhancing melt. The sum of these effects is that summer net radiation increases sharply toward the ice sheet margin. To resolve this correctly requires high-resolution climate models, in the order of 10 km or better.

Citation: van den Broeke, M., P. Smeets, J. Ettema, and P. K. Munneke (2008), Surface radiation balance in the ablation zone of the west Greenland ice sheet, *J. Geophys. Res.*, 113, D13105, doi:10.1029/2007JD009283.

1. Introduction

[2] With a surface area of 1.7 million km² and a volume representing a potential sea level rise of 7.3 m, the Greenland ice sheet (GrIS) is the largest source of fresh water in the Northern Hemisphere [Bamber *et al.*, 2001]. Each year, approximately 600 km³ of water equivalent accumulates on the ice sheet as snow, of which roughly half leaves the ice sheet as runoff after melting, the remainder being iceberg production from ice streams that terminate in fjords. The observed link between surface meltwater production and ice velocity [Zwally *et al.*, 2002] and the recent acceleration and thinning of several ice streams implies that the GrIS could already be a major contributor to the present-day sea level rise of 2.9 mm per year [Lemke *et al.*, 2007].

[3] The most important source for melt energy is radiation. The Greenland radiation climate is very variable in space and time [Konzelmann *et al.*, 1994; Knap and Oerlemans, 1996; Stroeve *et al.*, 2001]. To illustrate this, Figure 1, a MODIS scene of 23 August 2006, shows the ice-free Davis Strait, the snow-free tundra intersected by fjords

and Sukkertoppen Icecap in southwest Greenland. The ocean and ice-free tundra lakes have a low reflectivity for shortwave radiation or *albedo* ($\alpha < 0.1$). The snow-free tundra is slightly more reflective [$\alpha \approx 0.18$, Duynkerke and Vanden Broeke, 1994] while over the ice sheet, exposed glacier ice and superimposed ice in the ablation zone ($\alpha \approx 0.55$) are still appreciably darker than the dry snow surface in the interior ($\alpha \approx 0.85$), where melt occurs only sporadically. In winter the sea ice, tundra and ice sheet are covered by snow and have a uniformly high albedo ($\alpha \approx 0.80$ – 0.85).

[4] Because of the difficult working environment, with crevasses, meltwater percolation and refreezing and the formation of meltwater lakes [Box and Ski, 2007], only few experiments have been performed at the surface of the GrIS. The pioneering work of Ambach [1977] along the E.G.I.G. (Expédition Glaciologique Internationale au Groenland) profile was followed by meteorological expeditions in 1990 and 1991 by the ETH (Eidgenössische Technische Hochschule) Zürich at the equilibrium line near Paakitsoq, west Greenland [Greuell and Konzelmann, 1994]. In 1990 and 1991, the Institute for Marine and Atmospheric Research of Utrecht University and the Free University Amsterdam performed two climate experiments over tundra and ablation zone near Kangerlussuaq in west Greenland (Greenland Ice Margin Experiment, GIMEX90, GIMEX91 [Oerlemans and Vugts, 1993; Henneken *et al.*,

¹Institute for Marine and Atmospheric Research, Utrecht University (UU/IMAU), Utrecht, Netherlands.

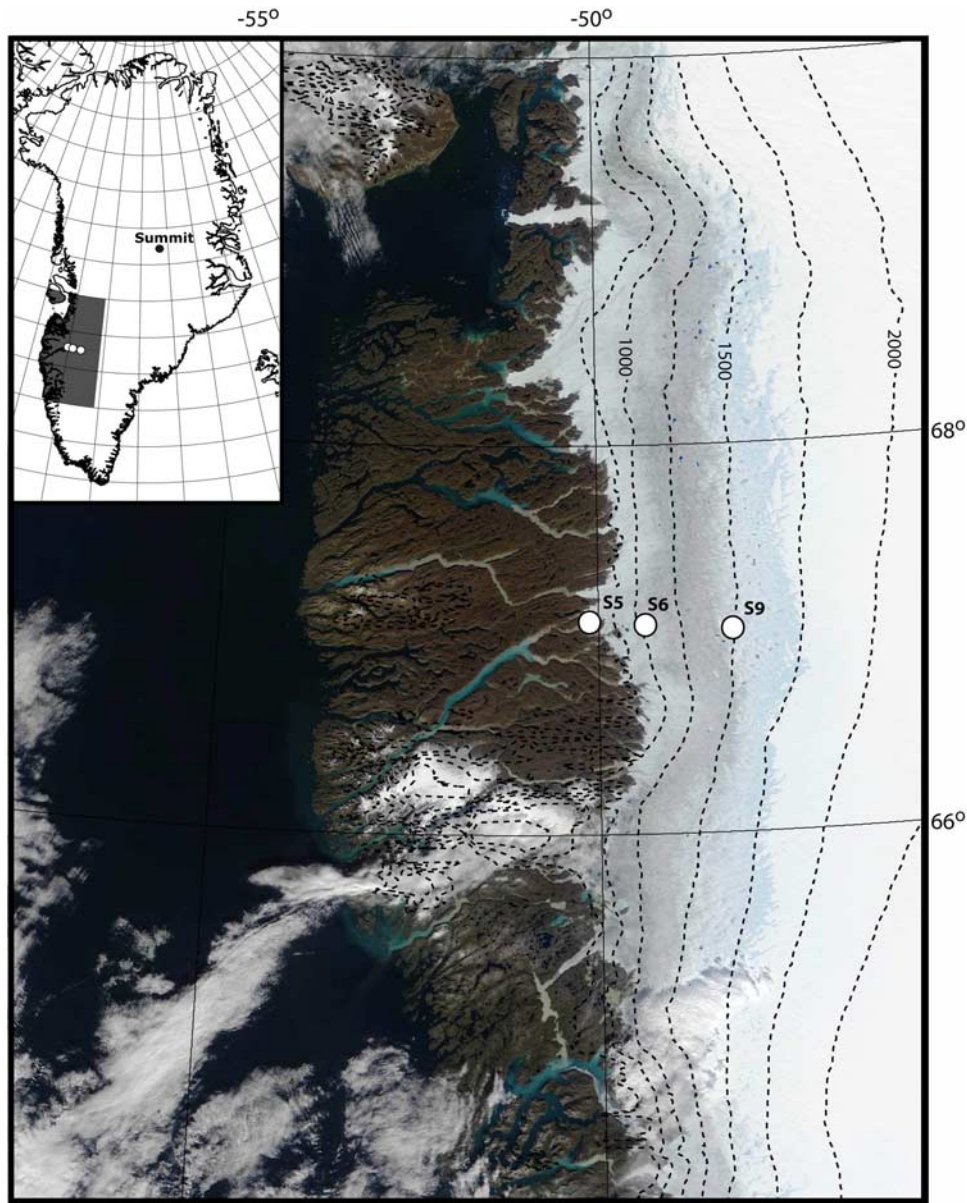


Figure 1. MODIS scene of west Greenland (23 August 2006) with AWS locations (white dots) and ice sheet elevation contours (dashed lines, height interval 250 m, from Bamber and others, 2001). Inset shows location of summit.

1994; Van de Wal and Russell, 1994]). This marked the start of mass balance measurements along the Kangerlussuaq transect, which are still continued today [Van de Wal et al., 2005]. In 2001–2003, the ETH conducted detailed year-round boundary layer observations at Summit, after which precise radiation measurements are continued in the framework of the Baseline Surface Radiation Network (BSRN [Ohmura et al., 1998]). Several aircraft-based studies have also been performed, notably KABEG in 1997 (Katabatic Wind and Boundary Layer Front Experiment around Greenland [Heinemann, 1999]) and IGLOS in 2002 (Investigation of the Greenland Boundary Layer at Summit [Drüe and Heinemann, 2003]). Konzelmann and Braithwaite [1995] and Bøggild et al. [1994] performed mass and energy balance studies in northeast Greenland.

[5] As most of the experiments listed above were summer-only, few year-round observations exist from the ice sheet surface. To improve this, automatic weather stations (AWS) are increasingly being used. In 1995, the Greenland Climate Network (GC-Net), coordinated by CIRES (Cooperative Institute for Research in Environmental Sciences), started off as part of the NASA funded Program for Arctic Regional Climate Assessment (PARCA). GC-Net presently consists of over 15 AWS along the 2000 m height contour as well as in the ablation zone in north and west Greenland [Steffen and Box, 2001]. As a contribution to this network, UU/IMAU installed three AWS along the Kangerlussuaq transect in southwest Greenland in August 2003. These AWS are equipped with Kipp & Zonen CNR1 radiation sensors.

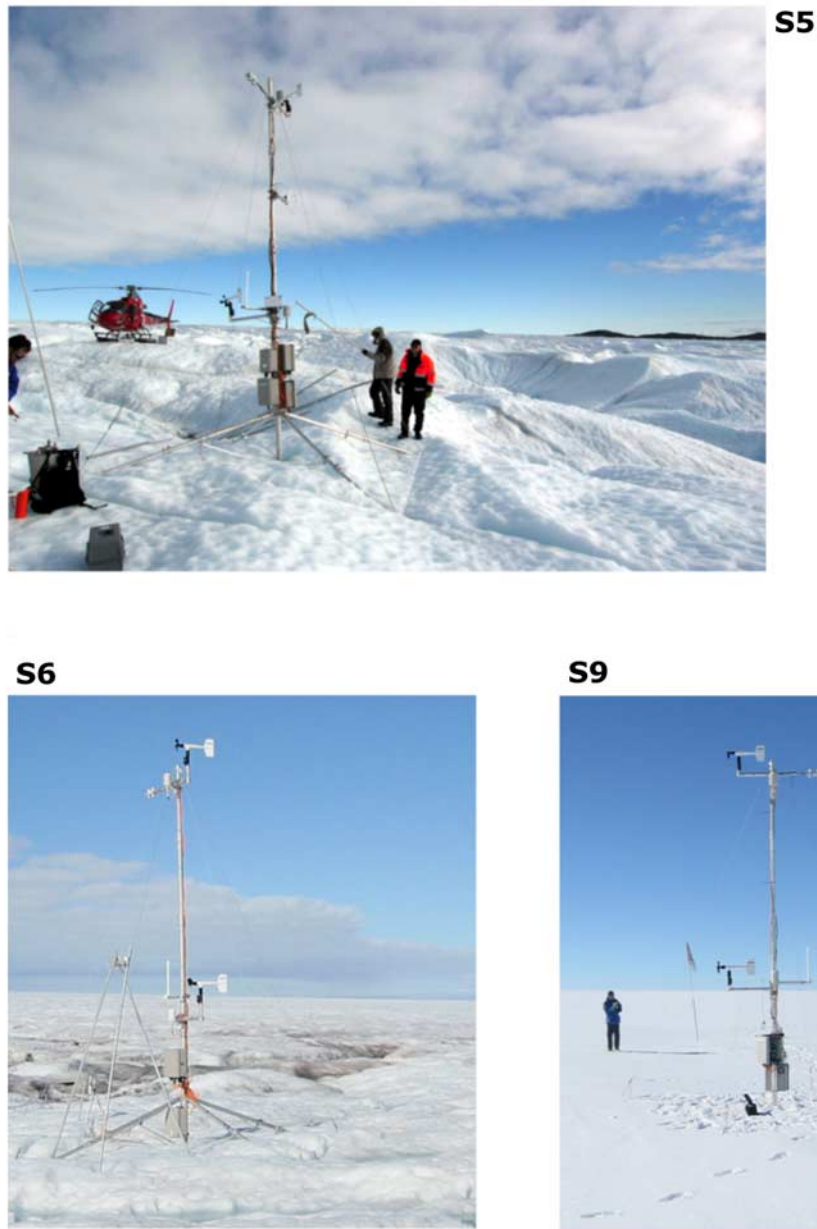


Figure 2. Images of AWS locations at S5 (27 August 2006), S6 and S9 (both 26 August 2006).

[6] Here we present the first 4 years of radiation data (September 2003–August 2007) from these AWS. In section 2 we describe methods, instruments and data treatment followed by results and discussion in section 3 and a summary and conclusions in section 4.

2. Methods

2.1. Radiation Balance

[7] The surface radiation balance can be written as:

$$\begin{aligned}
 R_{\text{net}} &= SW_{\text{net}} + LW_{\text{net}} \\
 &= SW_{\downarrow} + SW_{\uparrow} + LW_{\downarrow} + LW_{\uparrow} \\
 &= SW_{\downarrow} (1 - \alpha) + \varepsilon LW_{\downarrow} - \varepsilon \sigma T_s^4
 \end{aligned}
 \tag{1}$$

where fluxes toward the surface are defined as positive, R_{net} is net radiation absorbed at the surface, SW_{\downarrow} , SW_{\uparrow} , LW_{\downarrow} , LW_{\uparrow} are the downward and upward directed fluxes of shortwave and longwave radiation, α is the broadband surface albedo for SW radiation defined as $\alpha = -SW_{\uparrow}/SW_{\downarrow}$ (from now on referred to as “albedo”), ε the surface emissivity for longwave radiation (assumed to be 1.0), σ Stefan Boltzmann’s constant and T_s the surface “skin” temperature.

2.2. AWS Description and Sensor Specifications

[8] The AWS are situated at sites S5 (490 m asl), S6 (1020 m asl) and S9 (1520 m asl) of the Kangerlussuaq transect, a mass balance stake array that extends from the ice margin to 1800 m asl [Van de Wal *et al.*, 2005]. In Figure 1,

Table 1. AWS Sensor Specifications. EADT = Estimated Accuracy for Daily Totals

Sensor	Type	Range	Accuracy
Air pressure	VaisalaPTB101B	600 to 1060 hPa	4 hPa
Air temperature	Vaisala HMP35AC ^a	-80 to +56°C	0.3°C
Relative humidity ^a	Vaisala HMP35AC	0 to 100%	2%, (RH < 90%) 3 %, (RH > 90%)
Wind speed ^b	young 05103	0 to 60 m s ⁻¹	0.3 m s ⁻¹
Wind direction	young 05103	0 to 360°	3°
Pyranometer	Kipp en Zonen CM3	305 to 2800 nm	EADT ± 10%
Pyrgeometer	Kipp en Zonen CG3	5000 to 50000 nm	EADT± 10%
Snow/ice height	Campbell SR50	0.5 to 10 m	0.01 m or 0.4%

^aUnventilated.^bStarting speed ~ 1 m s⁻¹.

we can distinguish the bare ice zone (greyish, between 500–1500 m asl), the superimposed ice zone (milky blue, 1500–1750 m asl) and the snow covered percolation zone (bright white, 1750 m asl and higher). The dry snow zone is situated higher up the ice sheet and not visible in this image.

[9] Figure 2 shows the AWS and their surroundings in August 2006, near the end of the ablation season. The surface at S5 is very irregular with large hummocks, while at S6 and S9 the surface is aerodynamically smoother [Van den Broeke, 1996; Smeets and Van den Broeke, 2008]. The stations are designed such that they sink with the ablating surface. A sonic height ranger is attached to three stakes that are fixed in the ice to monitor surface height changes.

[10] The AWS are equipped with Kipp & Zonen (K&Z) CNR1 net radiometers, mounted at approximately 6 m above the surface to increase the field of view. The CNR1 sensor contains two K&Z CM3 pyranometers for downward and upward broadband shortwave radiation flux (spectral range 305–2800 nm) and two K&Z CG3 pyrgeometers for downward and upward broadband longwave radiation flux (spectral range 5000 to 50,000 nm). The K&Z CM3 is a thermopile type pyranometer, covered by a single glass dome, which complies with ISO 9060 second-class specifications (estimated accuracy for daily totals ±10%, Table 1). The K&Z CG3 pyrgeometer consists of a thermopile sensor covered by a silicon window that is transparent for far-

infrared radiation but absorbs solar radiation. No international standard exists for pyrgeometers; the factory-provided estimated accuracy of the K&Z CG3 for daily totals is ±10%. Because of energy considerations, the sensors are unventilated and unheated.

[11] Van den Broeke et al. [2004a] compared radiation measurements of the K&Z CNR1 with radiation data collected at Neumayer station, a Baseline Surface Radiation Network (BSRN, see www.bsrn.ethz.ch) station in Antarctica (70.7°S, 8.4°W, 50 m asl) for a 10-d period in February 2001. The comparison yielded a root mean squared difference of 2.7% (4.8 W m⁻²) for daily mean SW↓ and only 1.2% (2.7 W m⁻²) for daily mean LW↓. This leads to errors in monthly means < 1%, which shows that even under polar conditions the K&Z CM3 and CG3 typically perform much better than their specifications.

[12] Apart from atmospheric radiation, the AWS measure basic meteorological variables like wind speed and direction, temperature, relative humidity and air pressure (Table 1). Most variables, including radiation, are sampled at 6-min intervals (instantaneous, except for wind speed, cumulative) after which 1-h averages are stored in a Campbell CR10 data logger with separate memory module.

[13] In this paper we present the first 4 years of radiation data from these AWS (September 2003 to August 2007).

Table 2. AWS Topographic, Observational and Climate Characteristics

	S5	S6	S9	Summit
	<i>Location (Aug 2006)</i>			
Latitude, °N	67°06′	67°05′	67°03′	72°58′
Longitude, °W	50°07′	49°23′	48°14′	38°46′
Elevation, m asl	490	1020	1520	3203
Distance from ice edge, km	6	38	88	-
	<i>Period of Operation Used for This Paper</i>			
Start of observation	28 Aug 2003	1 Sep 2003	1 Sep 2003	1 Jul 2000
End of observation	27 Aug 2007	31 Aug 2007	31 Aug 2007	31 Dec 2004 ^a
	<i>Basic Climate Variables</i>			
Mass balance, m w.e.	-3.6	-1.5	~0	-
6 m temperature, K	267.7	263.4	260.6	244.7 ^b
Surface temperature, K	265.1	261.7	259.3	242.5
6-m relative humidity, %	75	87	90	-
6-m specific humidity, g kg ⁻¹	2.4	2.2	1.9	-
6-m wind speed, m s ⁻¹	5.0	6.4	7.3	4.1

^aAugust 2002 to May 2003 missing.^bMeasured at 2 m.

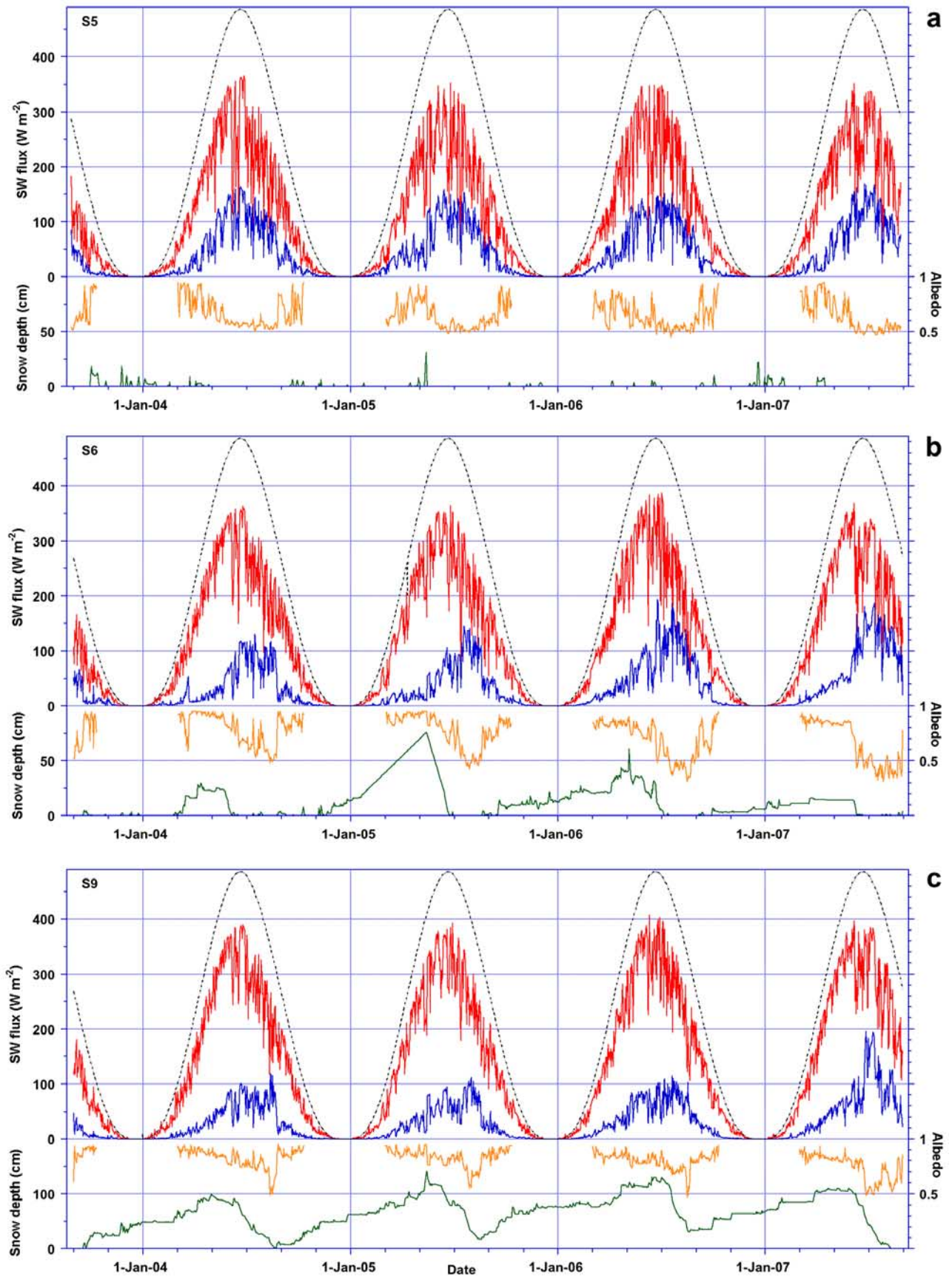


Figure 3. Daily mean values of SW_{TOA} , SW_{\downarrow} , SW_{net} , albedo, and snow depth at (a) S5, (b) S6, and (c) S9.

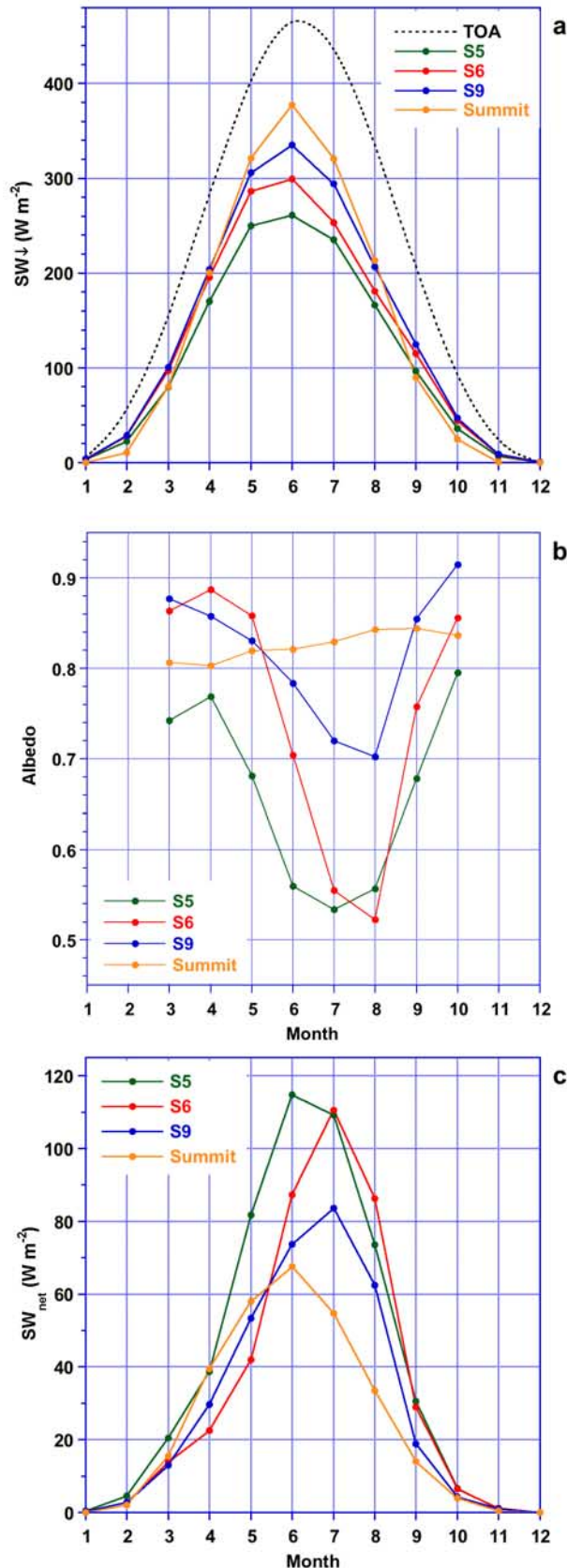


Figure 4. Average seasonal cycle, based on monthly means, of (a) SW_{TOA} and SW_{\downarrow} , (b) surface albedo, and (c) SW_{net} .

For reference, we also present radiation balance data from Summit, situated in the dry snow zone to the northeast (Figure 1), collected during the period July 2000 to July 2002 and June 2003 to December 2004 [Hoch, 2005; A. Ohmura, personal communication, 2008].

2.3. AWS Data Corrections

[14] Several corrections were applied to the radiation data. At S5 and S6, SW_{\downarrow} and SW_{\uparrow} were influenced by mast tilt. To correct this, first the minimum diffuse fraction of SW_{\downarrow} was estimated using the clear-sky scattering expression of *Atwater and Brown* [1974]. Next, the total diffuse fraction was estimated using LW_{\downarrow} following the method described by *Van den Broeke et al.* [2004a]. Finally, the correction of *MacWhorther and Weller* [1991] was applied to the direct fraction of SW_{\downarrow} and diffuse fractions of SW_{\downarrow} and SW_{\uparrow} . Tilt of the mast was measured during yearly maintenance visits, typically at the end of August. For data correction, this tilt is assumed to have been constant throughout the preceding ablation season.

[15] It was found that the K&Z CM3 measuring SW_{\uparrow} at S6 had a constant calibration offset; post-deployment recalibration of the sensor at the UU/IMAU test site using a K&Z CM21 as reference sensor showed that using a constant calibration offset solved this problem. At S9, the internal thermistor of the K&Z CNR1, which is used to calculate the LW fluxes, did not function from 23 June 2004 to 23 August 2005. Fortunately, this temperature could be accurately reconstructed (better than 1°C) using AWS air temperature and a correction for sensor heating under conditions of low wind speed and high insolation. In spite of the absence of heating and ventilation, icing/riming of the K&Z CNR1 appears to be no serious problem: katabatic winds maintain a continuous supply of adiabatically heated, unsaturated air which keeps the sensors free of ice.

[16] Snow depth was determined by first detecting the ice horizon, using albedo, and assigning subsequent increases of surface height to snow accumulation. Snow height data at S6 are missing for the spring of 2005: maximum snow height, onset and rate of snowmelt were estimated using an energy balance model, and snow height was linearly interpolated in between.

2.4. Calculation of Cloud Optical Thickness and Cloud Effect

[17] Information about clouds is valuable for a correct interpretation of temporal and spatial variability of radiation fluxes. Cloud optical thickness can be estimated from SW radiation measurements using the expression of *Fitzpatrick et al.* [2004]:

$$Trc = \frac{c_1(\tau) + c_2(\tau) \cos \theta}{1 + \tau(c_3 - c_4 \alpha)} \quad (2)$$

where Trc is the ratio of clearsky and actual SW_{\downarrow} , τ = the effective cloud optical depth, θ = solar zenith angle, α = surface albedo and c_1 , c_2 are factors depending on τ , the functional form of which is given by *Fitzpatrick et al.* [2004], while c_3 , c_4 are constants. The effective cloud optical depth is representative for a uniform cloud cover consisting of cloud droplets with a standard effective radius of 8.6 μm . Because θ , Trc and α are known, we can solve

Table 3. Mean Annual and Summer (June, July, August) Radiation Fluxes at the Three AWS and Summit

	S5	S6	S9	Summit
Start of observation	28 Aug 2003	1 Sep 2003	1 Sep 2003	1 Jul 2000
End of observation	27 Aug 2007	31 Aug 2007	31 Aug 2007	31 Dec 2004 ^a
		<i>Annual Means</i>		
SW↓ (W m ⁻²)	110	126	138	136
SW↑ (W m ⁻²)	-70	-92	-110	-114
SW _{net} (W m ⁻²)	40	33	28	22
LW↓ (W m ⁻²)	246	229	225	166
LW↑ (W m ⁻²)	-281	-268	-259	-196
LW _{net} (W m ⁻²)	-36	-39	-34	-30
R _{net} (W m ⁻²)	4	-6	-5	-7
		<i>Summer Means (JJA)</i>		
SW↓ (W m ⁻²)	220	244	278	303
SW↑ (W m ⁻²)	-121	-149	-205	-253
SW _{net} (W m ⁻²)	99	95	73	50
LW↓ (W m ⁻²)	293	272	267	215
LW↑ (W m ⁻²)	-315	-312	-306	-256
LW _{net} (W m ⁻²)	-22	-39	-40	-40
R _{net} (W m ⁻²)	77	56	33	10

^aAugust 2002 to May 2003 missing.

equation (2) for hourly values of τ . To improve accuracy, it was imposed that $\theta < 85^\circ$. For days with more than 12 available hourly values of τ , daily average τ was calculated. Next, these daily average τ values were regressed to fractional cloud cover calculated from LW↓ observations as outlined by *Van den Broeke et al.* [2004a]. A good correlation was found for all three AWS ($R = 0.78$ to 0.86), enabling us to use daily average LW↓ to calculate τ throughout the year.

[18] The cloud effect is defined as the difference in net radiation between average and clear-sky conditions. To calculate the cloud effect, we defined $\tau < 2$ to represent clearsky conditions, which represent 10–15% of the data ($N \sim 180$ d). This threshold was also used by *Fitzpatrick et al.* [2004] and strikes a balance between selecting conditions with no or little clouds while still retaining sufficient data for averaging. Using $\tau < 3$ would give more cloudy, so less reliable results, while choosing $\tau < 1$ would leave us with $N = 60$ d, too few to calculate a seasonal cycle. Obviously, a general problem is that the choice of the “clear sky” threshold impacts on the magnitude of the calculated cloud effect (see next section), which therefore should be interpreted qualitatively rather than quantitatively.

3. Results

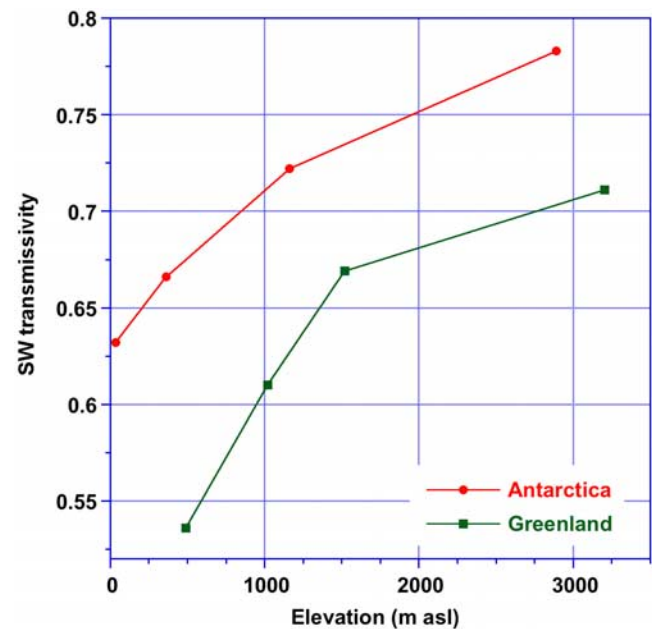
3.1. General Meteorological Conditions

[19] Table 2 lists the main topographical and annual climate/mass balance characteristics of the AWS sites. On

Table 4. Annual Mean Effective Cloud Optical Depth and Cloud Effect (see Text)

	S5	S6	S9
Effective cloud optical depth τ	9.0	8.4	8.0
SW cloud effect, W m ⁻²	-12	-7	-10
LW cloud effect, W m ⁻²	+37	+33	+30
Total cloud effect, W m ⁻²	+24	+26	+20

the basis of the sonic height ranger data, S5 and S6 experience a net annual ablation of -3.6 and -1.5 m w.e., respectively, while S9 is close to the equilibrium line. The influence of katabatic winds is visible in the decreasing relative humidity at lower elevations. The surface to air temperature gradient increases toward the ice margin, indicative of enhanced turbulent sensible heat exchange. The decreasing wind speed toward the ice margin mainly reflects an increased surface roughness at S5 during summer [*Smeets*

**Figure 5.** Annual mean atmospheric SW transmission (SW_{\downarrow}/SW_{TOA}) as a function of elevation for four AWS in Dronning Maud Land, East Antarctica (1998–2001) and the Greenland AWS (2003–2007).

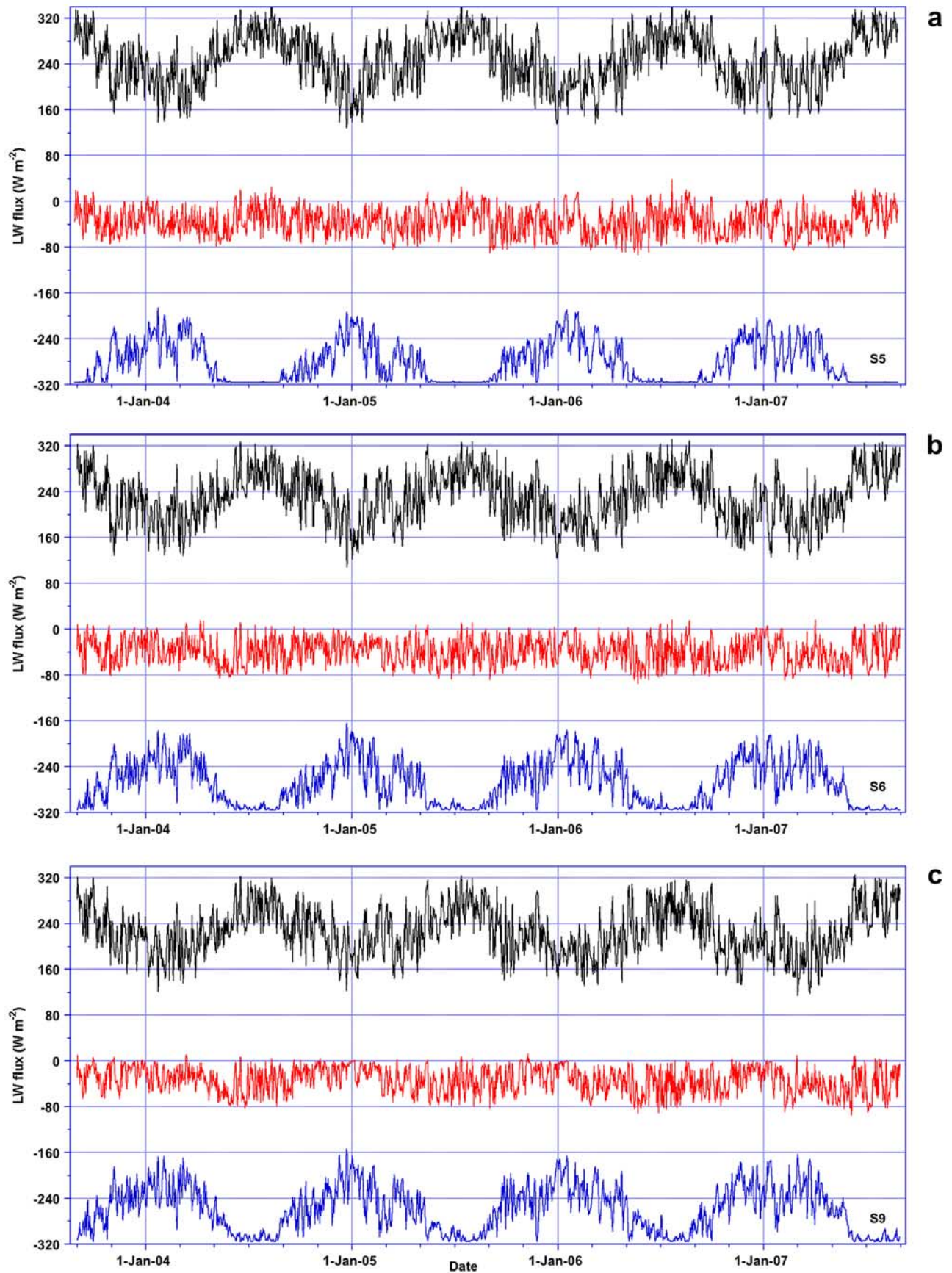


Figure 6. Daily mean values of LW_↓, LW_{net}, and LW_↑ at (a) S5, (b) S6, and (c) S9.

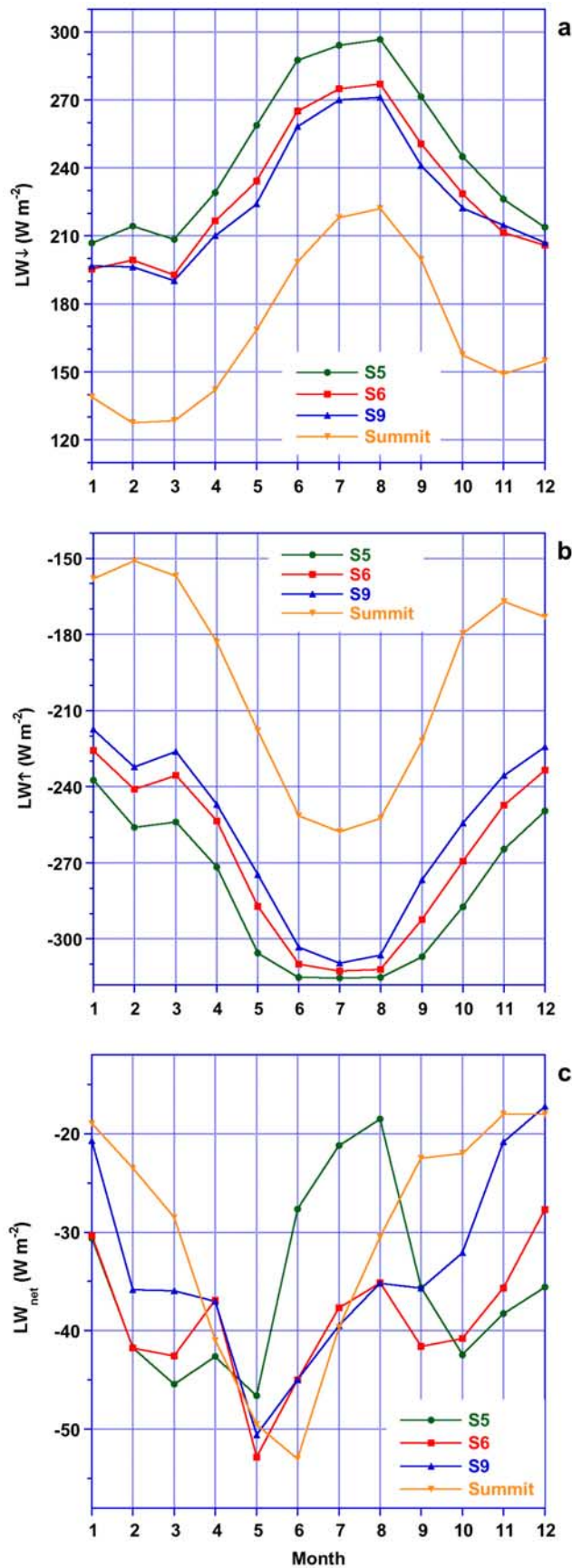


Figure 7. Average seasonal cycle, based on monthly means, of (a) LW_{\downarrow} , (b) LW_{\uparrow} , and (c) LW_{net} .

and Van den Broeke, 2008, Figure 2], which lowers the wind speed at AWS level.

3.2. Shortwave Radiation

[20] Figures 3a–3c show daily mean values of incoming shortwave radiation at the top of the atmosphere (SW_{TOA}) and at the surface (SW_{\downarrow} and SW_{net}), as well as albedo (α) and snow height. Albedo is only shown if $SW_{TOA} > 100 \text{ W m}^{-2}$. Figure 4 shows the seasonal cycles based on monthly means, of (a) SW_{TOA} and SW_{\downarrow} , (b) albedo, and (c) SW_{net} . Table 3 lists summer (JJA) and annual means.

[21] A remarkable feature in Figure 3a is that a continuous snow cover does not build up at S5 during winter. Instead, we see a series of shallow and short-lived snow covers. The most probable explanation is that snow that falls in winter is redistributed and collects in the crevasses and gullies that are typical for this part of the ice sheet (Figure 2). As the AWS and the snow height sensor are situated on a small ice hill, average snow depth may be underestimated. The radiation sensor is mounted at 6 m high in the mast, and has a field of view that includes the gullies surrounding the ice hill. The observed albedo is therefore representative of a larger area. This is confirmed by albedo values that are often higher than that of ice ($\alpha \approx 0.55$), even if the height sensor detects no snow. The fact that at S5 typical ice albedo values are reached already early in spring, even before the onset of melt, confirms that winter snow accumulation is small at the ice sheet margin.

[22] At S6 (Figure 3b), the winter snowpack is typically 20–70 cm deep. Surface albedo decreases gradually during June and July when the winter snow melts. An exception is the spring of 2004, where albedo starts out at the lower ice value after a winter without significant accumulation, and sharply increases after the first snowfall in March. The surface at S6 becomes snow-free typically in the beginning of July and remains so for about 6 weeks, apart from sporadic summer snowfall events that temporarily increase surface albedo and reduce ice melt. Note that with values < 0.4 the albedo at S6 in the summers of 2006 and 2007 is significantly lower than at S5, resulting in high values of SW_{net} . This agrees with the “dark band” identified by Greuell [2000] in AVHRR imagery, which he ascribed to the abundance of meltwater at the ice sheet surface.

[23] At S9 (Figure 3c), winter accumulation is largest, 70–120 cm of snow. During the melt season, the albedo gradually decreases to 0.7, indicative of wet snow. After the winter snow has melted away, the superimposed ice horizon, representing refrozen meltwater (not glacier ice) from the previous summer, is briefly exposed at the surface in August. When this happens, albedo drops sharply. Judging from Figure 3, the albedo of superimposed ice is comparable to that of glacier ice, approximately 0.5, even though the two surface types can be easily distinguished visually (Figure 1). At S9, the summer of 2007 is different from the previous three years: after a period of prolonged clear skies and rapid melting, the superimposed ice horizon surfaces already in June, close to the summer solstice. This results in strongly enhanced values of SW_{net} .

[24] Atmospheric transmission of SW radiation, which depends on atmospheric mass, water vapor content, solar zenith angle, surface albedo (through multiple scattering between snow surface and cloud) and cloud optical thick-

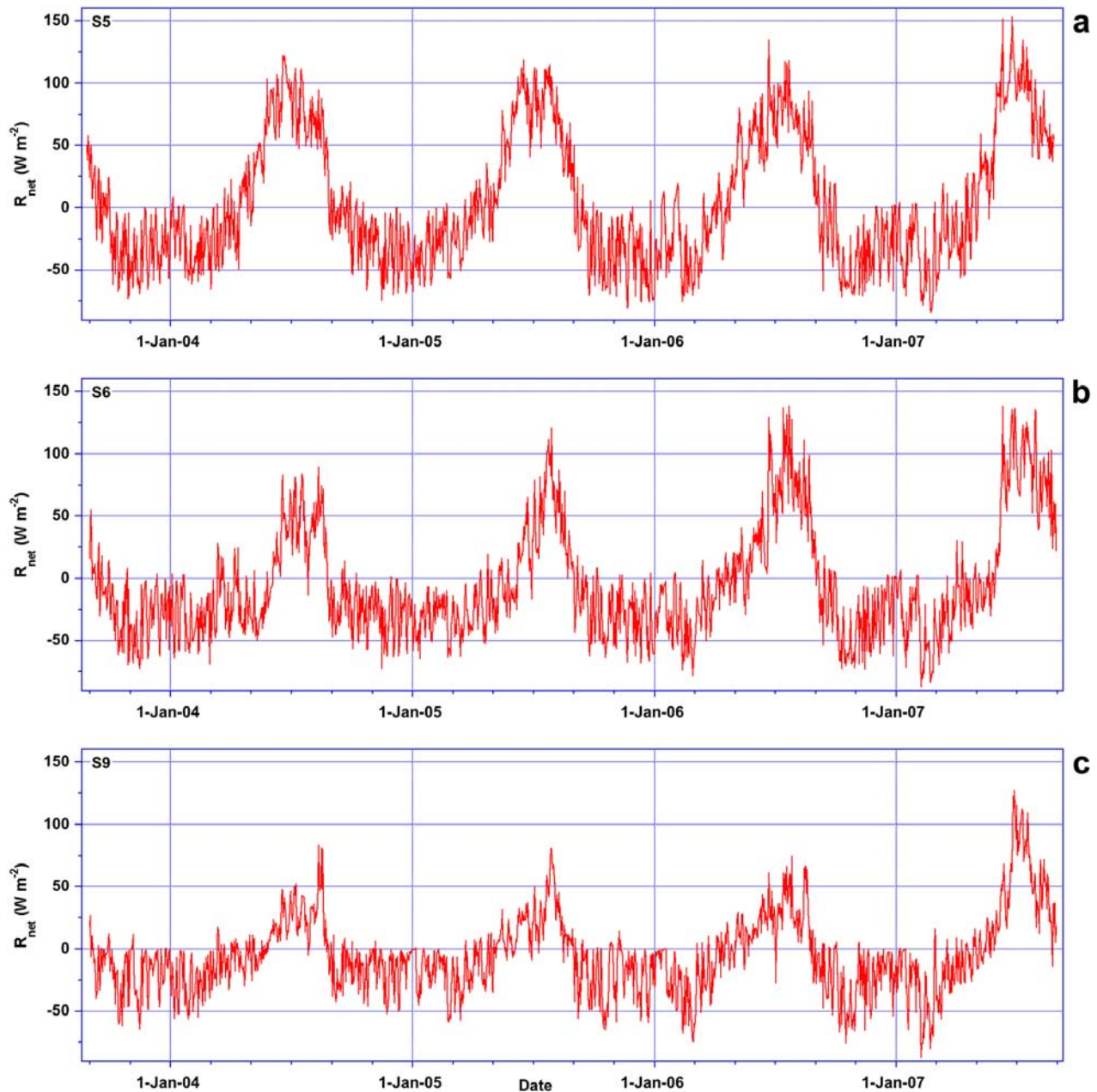


Figure 8. Daily mean values of R_{net} at (a) S5, (b) S6, and (c) S9.

ness, decreases quite sharply from the interior ice sheet toward the ice margin. The June average value of SW_{\downarrow} is 25% lower at S5 than at S9. Another notable feature is that SW_{\downarrow} in the ablation zone peaks well before the summer solstice. Increased cloud optical thickness in summer explains this asymmetry, as discussed in section 3.5.

[25] Albedo starts to decrease from April onwards at the sites in the ablation zone, i.e., before the onset of melt (Figure 4b). This is associated with the decrease in solar zenith angle. S5 starts out with a considerably lower April value (0.75) than the other two sites (0.85 to 0.9), reflecting the mixed surface of snow and glacier ice. At S5, the ice albedo value (~ 0.55) is reached already early in June, one

month before S6. At S9, monthly mean albedo decreases gradually and reaches a minimum in August. At Summit, a gradual increase in albedo occurs during the summer, in response to increased cloudiness [Hoch, 2005]. Clouds alter the spectral composition of SW_{\downarrow} toward shorter, higher albedo wavelengths [Wiscombe and Warren, 1980] and enhance multiple scattering.

[26] The combined effect of clouds and albedo is that SW_{net} reaches a maximum value in June at S5 and Summit but later at S6 and S9 (Figure 4c). The seasonal cycles of SW transmission and surface albedo work together to enhance/reduce absorbed SW radiation in the beginning of the melt season in lower/higher parts of the ablation zone.

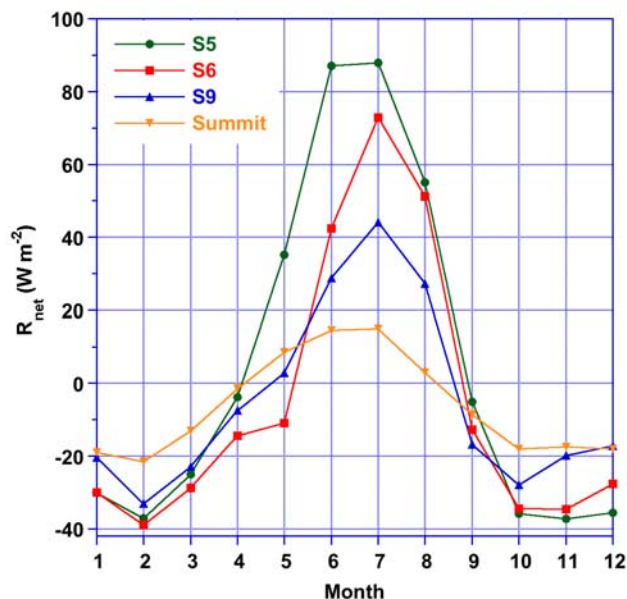


Figure 9. Average seasonal cycle, based on monthly means, of R_{net} .

Therefore the annual mean SW_{net} (Table 3) at S5 is 21% and 43% higher than at S6 and S9, respectively, in spite of the smaller atmospheric transmission for SW radiation. Comparing SW_{net} to SW_{TOA} (Table 4), we see that about 20% of incoming SW radiation at TOA is finally absorbed at the surface at S5, decreasing to 16% at S6, 14% at S9 and 12% at Summit.

[27] Figure 5 compares SW transmission in Greenland and Antarctica [Van den Broeke et al., 2004b]. The Greenland values are lower, owing to a greater cloud optical thickness and atmospheric moisture/aerosol load. The increasing difference at lower elevations stems from the higher surface albedo in Antarctica, where snow is at the surface throughout the year and melting is rare. This enhances multiple scattering between the surface and cloud base (Section 3.6).

3.3. Longwave Radiation

[28] Figure 6 shows daily means, Figure 7 the seasonal cycle and Table 3 annual and summer means of longwave radiation fluxes (LW_{\downarrow} , LW_{\uparrow} , and LW_{net}). LW_{\downarrow} is a measure for atmospheric temperature and emissivity, and the upper and lower extremes represent cloudy and clear conditions. The upper envelope of this curve is thus representative of cloud base temperature, the lower envelope a measure for clearsky emissivity and temperature [Konzelmann et al., 1994].

[29] When the surface has unit emissivity, as assumed here, LW_{\uparrow} is a direct measure for surface temperature. This results in much reduced variability during summer when the surface is at melting. At S5, melting is continuous from June to August, while at S6 and S9 melting is intermittent. Apart from short episodes in summer, LW_{net} represents a heat loss for the surface with daily mean LW_{net} as low as -80 W m^{-2} during clear summer days. The heat loss is smaller during

winter under temperature inversion conditions [Van den Broeke et al., 2004b].

[30] Figure 7a shows that LW_{\downarrow} peaks in August. The high values at S5 reflect the influence of the surrounding snow free tundra, above which air is heated by convection [Duynderke and Van den Broeke, 1994] and consequently advected over the protruding snout of Russell Glacier at which S5 is situated (Figure 1). Once over the ice sheet, the lower atmosphere adjusts its temperature to the melting ice surface leading to small differences in LW_{\downarrow} between S6 and S9.

[31] Combined with the fixed value for LW_{\uparrow} , at S5 the increasing LW_{\downarrow} in summer results in a pronounced August maximum in LW_{net} (Figure 7c). Summer mean cooling by LW_{net} is therefore limited to -22 W m^{-2} at S5 [Meesters and Van den Broeke, 1997], compared to $\sim -40 \text{ W m}^{-2}$ at the other two sites (Table 3). At S6 and S9, surface cooling by LW_{net} is strongest in May and June, when the snow surface is heated by the sun but has not yet reached the melting point. At S9, the smallest cooling by LW_{net} is found in the winter months November through January ($> -20 \text{ W m}^{-2}$), again as a result of the surface-based temperature inversion. In the annual mean (Table 3), LW_{net} is very similar among the sites (-30 to -39 W m^{-2}), but this is a coincidence given the different annual cycles.

3.4. Net Radiation

[32] Figure 8 shows daily means, Figure 9 the seasonal cycle and Table 3 the annual and summer means of net radiation R_{net} . Maximum daily mean R_{net} at S5 and S6 is around 120 W m^{-2} , representing summer conditions with little cloud cover over a relatively dark, melting ice surface. Interdiurnal variability is substantial, but the period with positive and negative R_{net} is well defined. The amplitude of the seasonal cycle of R_{net} (Figure 9) decreases from the margin onto the ice sheet. In the summer mean, R_{net} at S5 is 38% and 133% greater than at S6 and S9, respectively. In

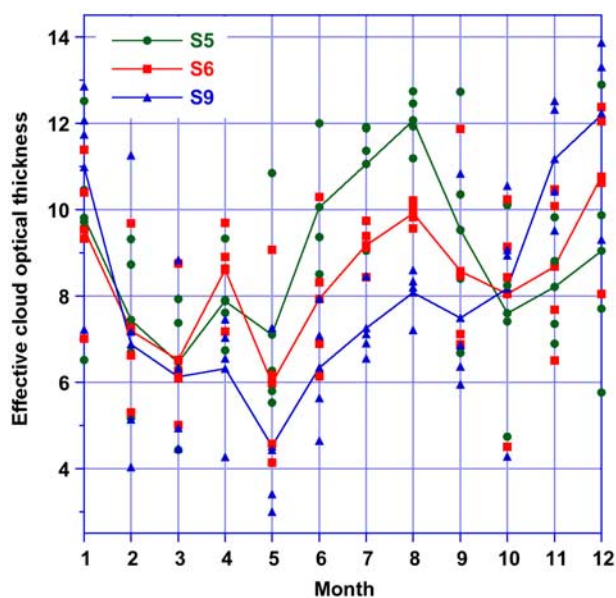
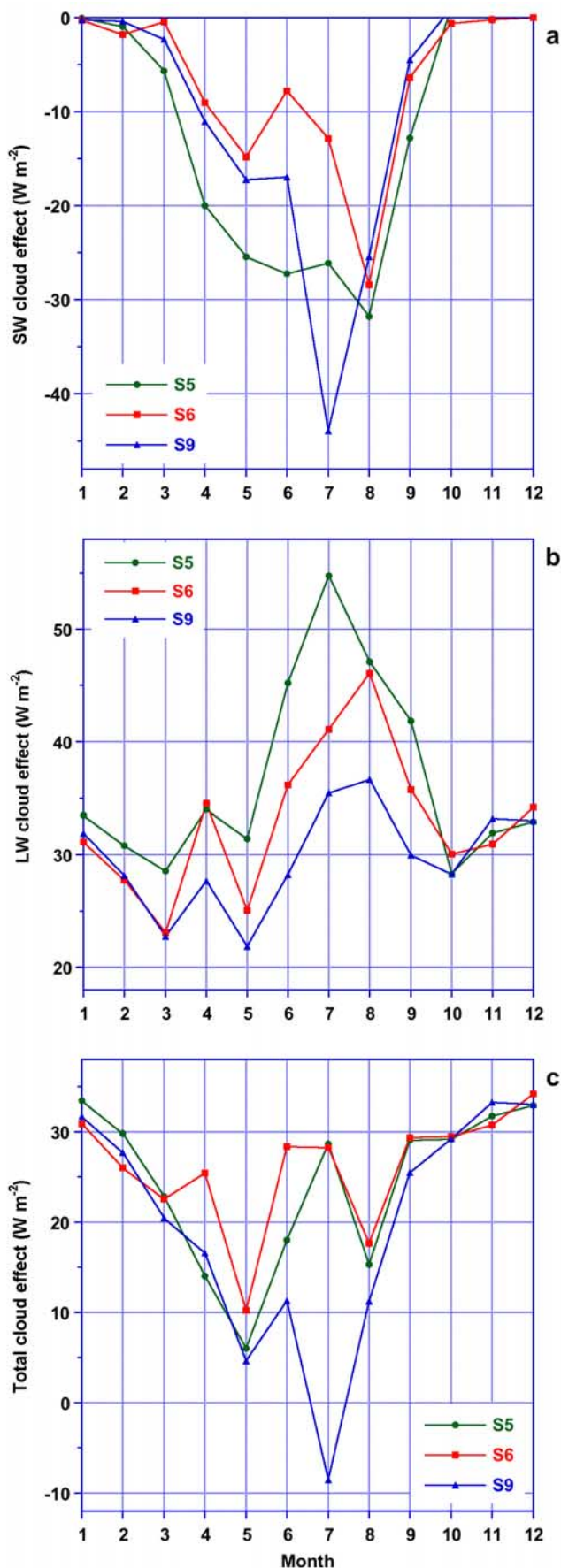


Figure 10. Average seasonal cycle, based on monthly means, of effective cloud optical thickness τ , with individual monthly values (2003–2007).



the annual mean, R_{net} is close to zero at all sites, with a small positive value at S5 and small negative values at S6, S9 and summit (Table 3).

3.5. Cloud Optical Depth and Cloud Effect

[33] Annual mean effective cloud optical depth (τ) decreases from 9.0 at S5 to 8.0 at S9 (Table 4). A notable feature is the increase of τ from May to August (Figure 10). While year-to-year differences are large for nonsummer months, the summer increase is a robust and yearly recurring feature, which has also been observed at Summit [Hoch, 2005]. This has important implications for the melt energy, because it means that, when albedo in the middle to higher ablation zone is at a minimum in late summer, the amount of $\text{SW}\downarrow$ available for melting is reduced by clouds.

[34] The magnitude of the cloud effect thus depends on many variables like average cloud cover, optical thickness, but also on e.g., surface albedo. Table 4 lists the annual mean SW, LW and total cloud effect. The total cloud effect is positive at all sites, i.e., clouds tend to increase R_{net} at the surface. This is sometimes referred to as the “radiation paradox” [Ambach, 1974], and is a result of the high surface albedo, which limits the (negative) SW cloud effect so that the (positive) LW cloud effect dominates the total cloud effect. Averaged over the year, the cloud effect is strongest at S6 and weakest at S9.

[35] Figure 11 shows the seasonal cycles of the SW, LW and total cloud effect. The SW cloud effect (Figure 11a) is strongest in July (S9) and August (S5 and S6), when clouds are abundant and surface albedo relatively low. The LW cloud effect (Figure 11b) also is strongest in these months, in response to thick clouds in combination with a melting surface that cannot further raise its temperature. Figure 11c shows that the radiation paradox exists in all months at all sites, except in July at S9.

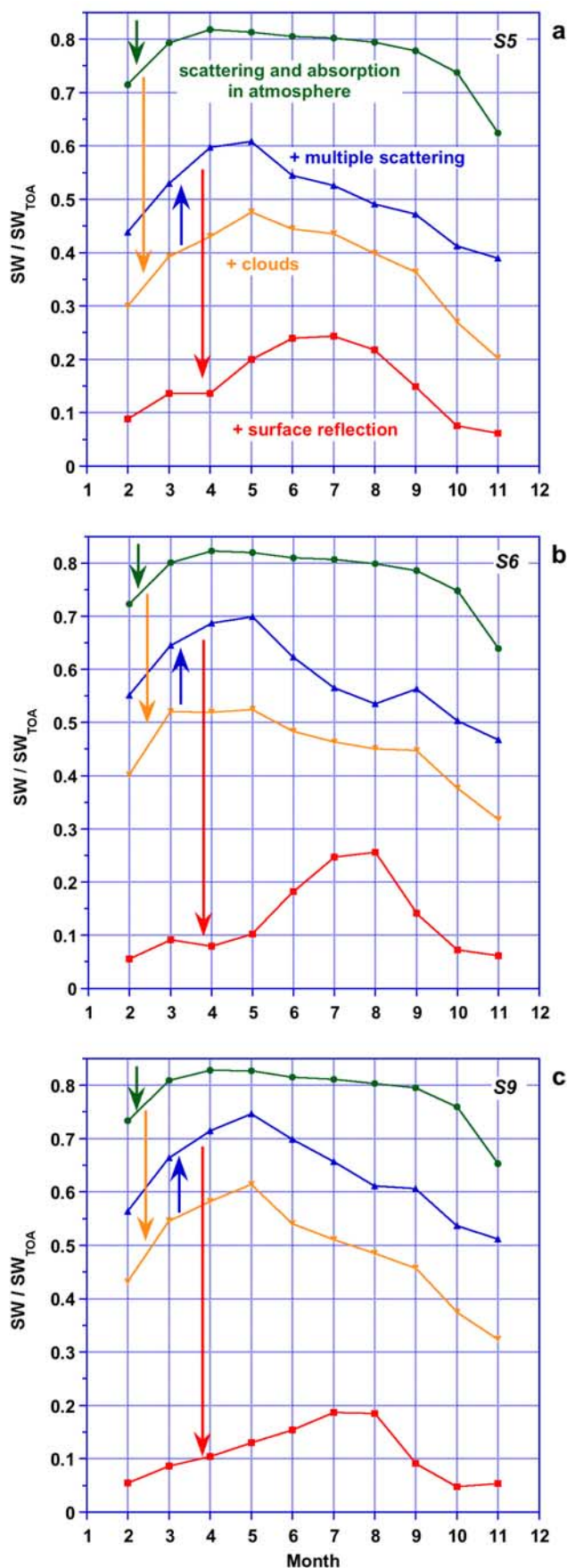
3.6. Factors Controlling SW_{net}

[36] SW_{net} represents the main energy source for snow and ice melt in Greenland, and is a critical parameter in calculating the present and future mass balance of the GrIS. Equation (2) enables us to isolate the various processes that influence SW_{net} .

- [37] 1. Scattering and absorption in the clear atmosphere
- [38] 2. Cloud scattering and absorption
- [39] 3. Multiple scattering between surface and cloud base
- [40] 4. Surface reflection

[41] Figure 12 shows the seasonal cycle of $\text{SW}\downarrow$, normalized by SW_{TOA} , after the stepwise allowance of the above listed processes, as indicated by the arrows. Table 5 lists the annual means, where values between brackets represent the absolute change in W m^{-2} relative to the previous step. At S5, for instance, clear-sky scattering and absorption decrease $\text{SW}\downarrow$ by 42 W m^{-2} . This effect is slightly smaller at S6 and S9. If we next allow for clouds but without multiple scattering between surface and cloud base (by setting $\alpha = 0$ in equation (2)), $\text{SW}\downarrow$ at S5 decreases further by 78 W m^{-2} . This reduction is significantly less at S6 and S9, where

Figure 11. Average seasonal cycle, based on monthly means, of (a) SW cloud effect, (b) LW cloud effect, and (c) total cloud effect. See text for more details.



summertime τ is smaller (Figure 10). If we take multiple scattering between surface and cloud base into account, SW_{\downarrow} is enhanced by 24 W m^{-2} (S5) to 29 W m^{-2} (S9). Finally, reflection at the surface reduces SW_{\downarrow} by 71 W m^{-2} at S5 to 110 W m^{-2} at S9. The overall result is that 14% (S9) to 20% (S5) of SW_{TOA} is absorbed at the ice sheet surface.

[42] Figure 12 shows that the effect of scattering and absorption in the clear atmosphere (green line) is strongest in spring and autumn, when the solar zenith angle is large. Also visible is a steady increase in SW absorption by water vapor. Adding the effect of scattering and absorption by clouds (without multiple scattering between the surface and cloud base) yields the orange line. SW_{\downarrow} now decreases monotonously from May onwards, which until August can be ascribed to increasing cloud optical depth. Adding the effect of multiple scattering (blue line) enhances the SW flux throughout the year, and decreases or even reverses the downward trend of SW_{\downarrow} in late summer. This is a result of the increase in surface albedo in response to accumulation of fresh snow and a larger solar zenith angle. Adding the effect of surface albedo gives observed SW_{net}/SW_{TOA} (red line). This last step accounts for the effects of the changing state of the surface (fresh snow \rightarrow old snow \rightarrow wet snow \rightarrow ice \rightarrow fresh snow etc.).

4. Summary and Conclusions

[43] We present 4 years of radiation observations and derived cloud properties from the ablation zone of the west Greenland ice sheet (GrIS) at 67°N . Data were collected using three automatic weather stations located at 6, 38, and 88 km from the ice sheet margin at elevations of 490, 1020, and 1520 m asl. A parameterization for the attenuation of downwelling shortwave radiation (SW_{\downarrow}) enabled us to deduce the effective cloud optical depth, and furthermore to isolate the effects of scattering and absorption by clouds and multiple scattering between ice sheet surface and cloud base.

[44] The SW balance at the surface of the GrIS is mainly determined by (1) the timing of the minimum in surface albedo and (2) the increase in cloud optical depth from May onwards. Surprisingly, a winter snow cover does not build up at the lowest site S5, where surface albedo maintains its lower ice value throughout the melting season. This enhances SW absorption in early summer, when cloud optical depth is still relatively small, and supports strong melting at the ice sheet margin. In the higher ablation zone, the winter snowpack is deeper and albedo reaches its minimum later in the ablation season (July/August). At this time, cloud optical depth has already increased resulting in markedly less absorbed SW .

[45] At the ice sheet margin (S5), incoming longwave radiation peaks in August in response to air that is heated over the snow free tundra. Because continuous surface

Figure 12. Average seasonal cycle, based on monthly means, of processes affecting SW_{\downarrow} transmission at (a) S5, (b) S6, and (c) S9. Arrows indicate the stepwise allowance of (1) clear-sky scattering and absorption, (2) cloud scattering and absorption, (3) multiple scattering between surface and cloud base, and (4) surface reflection.

Table 5. Annual Mean SW \downarrow , Normalized by SW $_{TOA}$, After the Stepwise Allowance of Processes 1–4, Indicated by the Arrows in Figure 12^a

	S5	S6	S9
SW $_{TOA}$, W m $^{-2}$	207	207	207
	<i>SW attenuation components</i>		
1. SW \downarrow /SW $_{TOA}$, clear-sky	0.80 (–42)	0.80 (–41)	0.81 (–40)
2. SW \downarrow /SW $_{TOA}$, clouds, $\alpha = 0$	0.42 (–78)	0.48 (–68)	0.53 (–59)
3. SW \downarrow /SW $_{TOA}$, clouds	0.54 (+24)	0.61 (+27)	0.67 (+29)
4. SW $_{net}$ /SW $_{TOA}$	0.20 (–71)	0.16 (–93)	0.14 (–110)

^aValues between brackets are absolute changes relative to previous step, in W m $^{-2}$.

melting in summer limits the amount of emitted longwave radiation, the total absorbed radiation at S5 exceeds that at S6 and S9 by 38% and 133%, respectively. Simulation of this steep gradient over horizontal distances <100 km requires high-resolution atmospheric modeling, in the order of 10 km or less, which can at present only be achieved by regional climate models.

[46] **Acknowledgments.** Three reviewers are thanked for comments. We thank the technical department and field parties of UU/IMAU for designing, building and maintenance of the AWS. This work was funded by Utrecht University and the Netherlands Polar Program (NPP).

References

- Ambach, W. (1974), The influence of cloudiness on the net radiation balance of a snow surface with a high albedo, *J. Glaciol.*, *13*, 73–84.
- Ambach, W. (1977), Untersuchungen zum Energieumsatz in der Akkumulationszone des Grönländischen Inlandeises, *Meddelelser om Grønland* 187–7, Bianco Lunos Bogtrykkeri A/S, Copenhagen.
- Atwater, M. A., and P. Brown Jr. (1974), Numerical calculation of the latitudinal variation of solar radiation for an atmosphere of varying opacity, *J. Appl. Meteorol.*, *13*, 289–297.
- Bamber, J. L., S. Ekholm, and W. B. Krabill (2001), A new, high-resolution digital elevation model of Greenland fully validated with airborne altimeter data, *J. Geophys. Res.*, *106*(B4), 6733–6745.
- Bøggild, C. E., N. Reeh, and H. Oerter (1994), Modelling ablation and mass-balance sensitivity to climate change of Storstrømmen, northeast Greenland, *Global Planet. Change*, *9*, 79–90.
- Box, J. E., and K. Ski (2007), Remote sounding of Greenland supraglacial melt lakes: Implications for subglacial hydraulics, *J. Glaciol.*, *53*(181), 257–265.
- Drüe, C., and G. Heinemann (2003), Investigation of the Greenland atmospheric boundary layer over summit 2002 (IGLOS), in *Reports on Polar and Marine Research*, vol. 447, 81 pp., Alfred-Wegener-Institute for Polar Research, Bremerhaven, FRG.
- Duynkerke, P. G., and M. R. van den Broeke (1994), Surface energy balance and katabatic flow over glacier and tundra during GIMEX-91, *Global Planet. Change*, *9*, 17–28.
- Fitzpatrick, M. F., R. E. Brandt, and S. G. Warren (2004), Transmission of solar radiation by clouds over snow and ice surfaces: A parameterization in terms of optical depth, solar zenith angle, and surface albedo, *J. Clim.*, *17*, 266–275.
- Greuell, W. G. (2000), Melt-water accumulation on the surface of the Greenland ice sheet: Effect on albedo and mass balance, *Geogr. Ann., Ser. A*, *82*(A4), 489–498.
- Greuell, W. G., and T. Konzelmann (1994), Numerical modelling of the energy balance and the englacial temperature of the Greenland Ice Sheet. Calculations for the ETH-Camp location (West Greenland, 1155 m a.s.l.), *Global Planet. Change*, *9*, 91–114.

- Heinemann, G. (1999), The KABEG'97 field experiment: An aircraft-based study of the katabatic wind dynamics over the Greenlandic ice sheet, *Boundary Layer Meteorol.*, *93*, 75–116.
- Henneken, E. A. C., N. J. Bink, H. F. Vugts, F. Cannemeijer, and A. G. C. A. Meesters (1994), A case study of the daily energy balance near the equilibrium line on the Greenland ice sheet, *Global Planet. Change*, *9*, 69–78.
- Hoch, S. (2005), Radiative flux divergence in the surface boundary layer: A study based on observations at Summit, Greenland, Ph.D. thesis, 180 pp., ETH Zürich, Switzerland.
- Knap, W. H., and J. Oerlemans (1996), The surface albedo of the Greenland ice sheet: Satellite-derived and in situ measurements in the Søndre Strømfjord area during the 1991 melt season, *J. Glaciol.*, *42*(141), 364–374.
- Konzelmann, T., and R. J. Braithwaite (1995), Variations of ablation, albedo and energy balance at the margin of the Greenland ice sheet, Kronprins Christian Land, eastern North Greenland, *J. Glaciol.*, *41*(137), 174–182.
- Konzelmann, T., R. S. W. van de Wal, W. Greuell, R. Bintanja, A. A. C. Henneken, and A. Abe-Ouchi (1994), Parameterisation of global and longwave incoming radiation for the Greenland ice sheet, *Global Planet. Change*, *9*, 143–164.
- Lemke, P., et al. (2007), Observations: Changes in snow, ice and frozen ground, in *Climate Change 2007: The Physical Science Basis. Contribution of Working Group I to the Fourth Assessment Report of the Intergovernmental Panel on Climate Change*, edited by S. Solomon et al., Cambridge Univ. Press, New York.
- MacWhorther, M. A., and R. A. Weller (1991), Error in measurements of incoming shortwave radiation made from ships and buoys, *J. Atmos. Oceanic Technol.*, *8*, 108–117.
- Meesters, A. G. C. A., and M. R. van den Broeke (1997), Response of longwave radiation above a melting surface to climate warming, *J. Glaciol.*, *43*, 66–70.
- Oerlemans, J., and H. F. Vugts (1993), A meteorological experiment in the melting zone of the Greenland ice sheet, *Bull. Am. Meteorol. Soc.*, *74*, 355–365.
- Ohmura, A., et al. (1998), Baseline Surface Radiation Network (BSRN/WRMC): New precision radiometry for climate research, *Bull. Am. Meteorol. Soc.*, *79*(10), 2115–2136.
- Smeets, C. J. P. P., and M. R. van den Broeke (2008), Temporal and spatial variation of momentum roughness length in the ablation zone of the Greenland ice sheet, *Boundary Layer Meteorol.*, in press.
- Steffen, K., and J. E. Box (2001), Surface climatology of the Greenland ice sheet: Greenland Climate Network 1995–1999, *J. Geophys. Res.*, *106*(D24), 33,951–33,964.
- Stroeve, J., J. E. Box, J. Maslanik, J. Key, and C. Fowler (2001), Intercomparison between in situ and AVHRR Polar Pathfinder-derived surface albedo over Greenland, *Remote Sens. Environ.*, *75*(3), 360–374.
- Van den Broeke, M. R. (1996), Characteristics of the lower ablation zone of the west Greenland ice sheet for energy-balance modelling, *Ann. Glaciol.*, *23*, 160–166.
- Van den Broeke, M. R., D. van As, C. H. Reijmer, and R. S. W. van de Wal (2004a), Assessing and improving the quality of unattended radiation observations in Antarctica, *J. Atmos. Oceanic.*, *21*(9), 1417–1431.
- Van den Broeke, M. R., D. van As, C. H. Reijmer, and R. S. W. van de Wal (2004b), The surface radiation balance in Antarctica as measured with Automatic Weather Stations, *J. Geophys. Res.*, *109*, D09103, doi:10.1029/2003JD004394.
- Van de Wal, R. S. W., and A. Russell (1994), A comparison of energy balance calculations, measured ablation and meltwater runoff near Søndre Strømfjord, West Greenland, *Global Planet. Change*, *9*, 29–38.
- Van de Wal, R. S. W., W. Greuell, M. R. van den Broeke, W. Boot, H. Snellen, C. H. Reijmer, and J. Oerlemans (2005), Mass balance measurements along a transect in West-Greenland over the period 1990–2003, *Ann. Glaciol.*, *42*, 311–316.
- Wiscombe, W. J., and S. G. Warren (1980), A model for the spectral albedo of snow. Part I: Pure snow, *J. Atmos. Sci.*, *37*, 2712–2733.
- Zwally, H. J., W. Abdalati, T. Herring, K. Larson, J. Saba, and K. Steffen (2002), Surface melt-induced acceleration of Greenland ice-sheet flow, *Science*, *297*, 218–222.

J. Ettema, P. K. Munneke, P. Smeets, and M. van den Broeke, Institute for Marine and Atmospheric Research, Utrecht University (UU/IMAU), P.O. Box 80005, 3508TA Utrecht, Netherlands. (broeke@phys.uu.nl)